Earth and Planetary Science Letters 395 (2014) 61–70

Contents lists available at ScienceDirect

Earth and Planetary Science Letters

www.elsevier.com/locate/epsl

The crust and uppermost mantle structure of Southern Peru from ambient noise and earthquake surface wave analysis

Yiran Ma *, Robert W. Clayton

Seismological Laboratory, California Institute of Technology, CA 91125, USA

ARTICLE INFO

Article history:
Received 17 December 2013
Received in revised form 7 March 2014
Accepted 8 March 2014
Available online xxxx
Editor: P. Shearer

Keywords:
Central Andes
flat subduction
surface wave tomography

ABSTRACT

Southern Peru is located in the northern Central Andes, which is the highest plateau along an active subduction zone. In this region, the Nazca slab changes from normal to flat subduction, with the associated Holocene volcanism ceasing above the flat subduction regime. We use 6 s to 67 s period surface wave signals from ambient noise cross-correlations and earthquake data, to image the shear wave velocity (V_{SV}) structure to a depth of 140 km. A mid-crust low-velocity zone is revealed, and is interpreted as partially molten rocks that are part of the Andean low-velocity zone. It is oblique to the present trench, and possibly indicates the location of the volcanic arcs formed during the steepening of the Oligocene flat slab beneath the Altiplano plateau. The recently subducted slab beneath the forearc shows a decrease in velocity from the normal to flat subduction regime that might be related to hydration during the formation of the Nazca ridge, which in turn may contribute to the buoyancy of the flat slab. The mantle above the flat slab has a comparatively high velocity, which indicates the lack of melting and thus explains the cessation of the volcanism above. A velocity contrast from crust to uppermost mantle is imaged across the Cusco–Vilcanota Fault System, and is interpreted as the boundary between two lithospheric blocks.

1. Introduction

Southern Peru is an interesting area to study subduction, orogeny and the related volcanism processes along an active continental margin. The dip of the subducted Nazca slab changes from 30° in the southeast to nearly horizontal at a depth of ∼100 km in the northwest (Fig. 1). Closely linked with the subduction process, the Quaternary volcanic arc is well developed where the slab is steeper and is absent where the slab is nearly flat (Allmendinger et al., 1997). This area is also characterized by the over 4 km high orogeny of the Central Andes. The high topography is widest above the normal subduction regime, and narrows considerably to the northwest over the flat subduction regime. From the coast to inland, the main tectonic units include the offshore and onshore forearc region, the Western Cordillera, the Altiplano plateau, and an eastern belt of fold and thrust structures comprising the Eastern Cordillera and the Sub-Andean Ranges (Fig. 1) (Oncken et al., 2006). The major crustal thickening is suggested to have initiated around 30–40 Ma (asynchronous for each tectonic unit), and is continuing to present (Mamani et al., 2010; Oncken et al., 2006).

Recent studies in Southern Peru using receiver functions (Phillips and Clayton, 2014; Phillips et al., 2012) suggest that the crustal thickness changes from ∼20 km near the coast to ∼70 km below the Altiplano plateau. The crustal P-wave structure under the plateau has been investigated by an active seismic survey along a profile from Peru to Bolivia, and is characterized by two low-velocity layers at 9–12 km and 36–46 km depth ranges (Ocola and Meyer, 1972). The deeper layer at the mid-crust depth is also detected in the receiver function (Yuan et al., 2000) and ambient noise surface wave (Ward et al., 2013), as well as other geophysical observations (Schilling et al., 2006) in the Central Andes, and is interpreted as a large volume of molten rocks (Schilling et al., 2006; Yuan et al., 2000). The extensive crustal melting can be attributed to the steepening of an Oligocene flat slab beneath the Altiplano plateau and an early Miocene flat slab beneath the Puna plateau (Kay and Coira, 2009; Ramos and Folguera, 2009). The mantle-wedge convection and arc volcanism resumed when the flat slab began to steepen, and because of the increase in the dip of the slab, the arc migrated trench-ward from inland to the present location (Allmendinger et al., 1997; Mamani et al., 2010) leading to widespread magmatism and heat input into the crust, which caused the crustal melting. While the magmatic addition is not as important as tectonic shortening to the crustal thickening, it had a

* Corresponding author.
E-mail address: yrma@caltech.edu (Y. Ma).

http://dx.doi.org/10.1016/j.epsl.2014.03.013

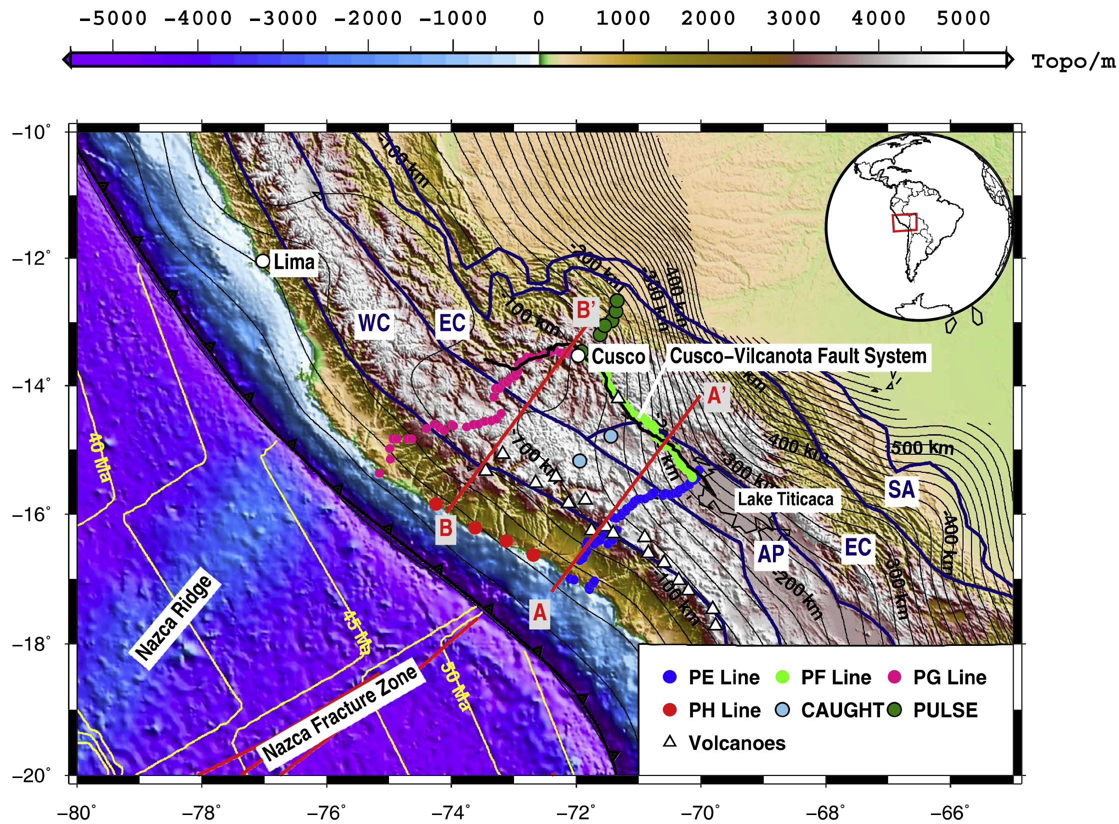

Fig. 1. Location of the seismic stations (dots) used in this study. The main units building the Central Andes are delineated with navy lines (modified from Oncken et al., 2006). WC: Western Cordillera; EC: Eastern Cordillera; AP: Altiplano Plateau; SA: Sub-Andean Ranges. The Holocene volcanoes are denoted with white triangles (data from http://www.volcano.si.edu/world). The thick black line is the Cusco–Vilcanota Fault System digitized from Carlier et al. (2005). Slab contours are from http://earthquake.usgs.gov/research/data/slab, plotted at 20 km intervals. The Nazca fracture zone data are from http://www.soest.hawaii.edu/PT/GSFML. Ocean floor age data are from http://www.earthbyte.org/Resources/Agegrid/2008/grids, plotted in 2.5 Ma intervals. Topography data are from http://glcf.umd.edu/data/srtm.

major effect on rheology and the mechanical behavior of the crust (Allmendinger et al., 1997).

The Peruvian flat subduction is not unique, as approximately 10 percent of present day subduction zones are considered to have flat slabs (Gutscher et al., 2000; Skinner and Clayton, 2013). Many of the present normal subduction regimes, such as the ones under Altiplano and Puna plateaux (Ramos and Folguera, 2009) mentioned above, are also considered to have experienced flat subduction in the past. The major driving forces of the flat subduction are still unknown, but some possible causes are summarized in Gutscher (2002), among which the subduction of thickened oceanic crust (e.g. the Nazca ridge and the Inca Plateau Gutscher et al., 1999) is suggested to be the dominant one. However, Skinner and Clayton (2013) argue through plate reconstructions that there is no clear correlation between the arrival of the thickened crust and the onset of slab flattening in South America. In addition, geodynamical modeling (Gerya et al., 2009) shows that the buoyancy of the thickened crust itself is not sufficient to raise the slab to the flat orientation, even including a less-dense depleted mantle associated with the formation of a thick crust (Abbott, 1991). The importance of the enhanced mantle wedge suction caused by the thick continental craton near the subduction zone is raised by several other studies (Manea et al., 2012; O'Driscoll et al., 2012). For example, O'Driscoll et al. (2012) suggested that the subduction towards the Amazonian Craton of South America, which is close to the trench, contributed to the flattening of the slab beneath the Altiplano plateau during the late Eocene and Oligocene, while the steepening of this Oligocene flat slab was associated with a change in the subduction direction, which resulted in a weakened wedge suction.

In this paper, we present the velocity structure in the crust and uppermost mantle from surface wave analysis. We show the extent of the mid-crust Andean low-velocity zone in the study region, the two lithosphere blocks across the Cusco–Vilcanota Fault System, and the velocity differences between the flat and normal subduction regimes. This study complements the receiver function studies of Phillips et al. (2012) and Phillips and Clayton (2014) that focuses on the velocity discontinuities (e.g. the Moho and slab depths) of this area.

2. Data and method

The data used in this study are primarily from a box-like array deployed progressively from June 2008 to February 2013 in Southern Peru (Fig. 1). The array is composed of ∼150 broadband stations (PE, PF, PG, PH lines), each with ∼2 yrs of deployment. We also use data from 8 broadband stations from the CAUGHT and PULSE experiments (Ward et al., 2013). We correct the data for the instrument response, integrate the velocity records to displacement, and use the vertical 1-sample/s channel to obtain the Rayleigh wave signals.

The phase velocity of Rayleigh wave is sensitive to the shear velocities over a range of depths, but is most sensitive to a depth range that is approximately one-third of its wavelength. By combining the phase velocities at various periods, we are able to invert for the shear wave velocity structure as a function of depth. For periods 6 s to 25 s, we use the surface wave signals from the ambient noise cross-correlations, and for 25 s to 67 s, we use the earthquake surface wave signals. We first make a phase velocity map of the area for each period and then perform a 1-D structure

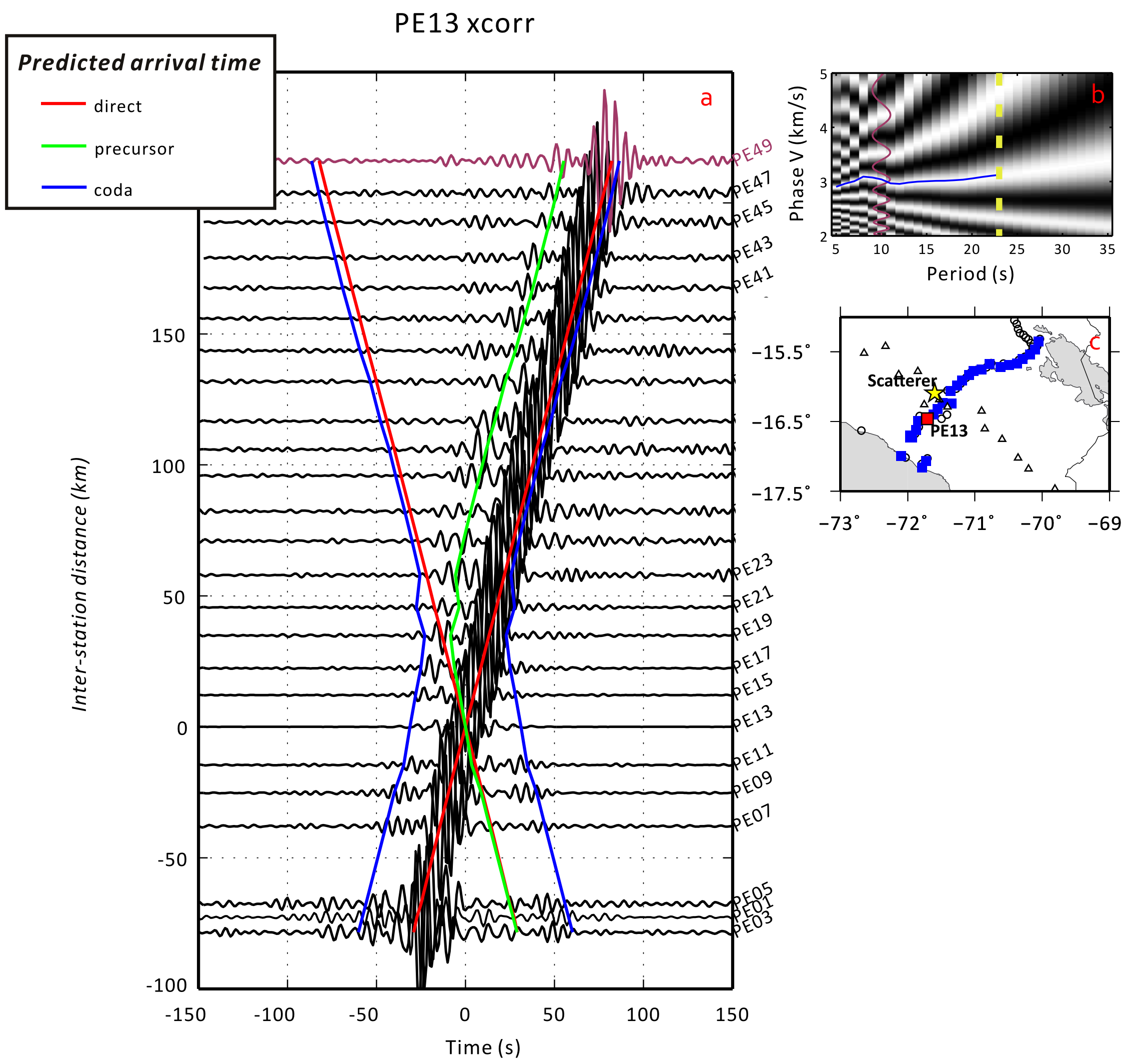

Fig. 2. (a) The cross-correlations between PE13 and all the odd number stations on PE line (see Panel c for the stations). The stations are numbered from the coast to inland. Also shown are the predicted arrival time of the precursor and coda waves due to the scatterer located in Panel c. (b) An example of measuring the dispersion curve of the cross-correlation between PE13 and PE49 (pink trace in Panel a). The yellow dashed line indicates the maximum period can be measured in order to satisfy the far field approximation (see text for more details). (c) The stations used in the cross-correlations in Panel a. Also shown is the location of the strong surface-wave scatterer (Ma et al., 2013). (For interpretation of the references to color in this figure legend, the reader is referred to the web version of this article.)

inversion on the dispersion curve at each location on the map. The 1-D structures are then combined to make a 3-D structure.

2.1. Ambient noise

The surface wave portion of the ambient noise cross-correlations has been used extensively to determine the earth structure (Brenguier et al., 2007; Lin et al., 2008; Shapiro et al., 2005; Yao et al., 2006). Here, we use a similar method to Bensen et al. (2007) to perform vertical–vertical cross-correlations between all station pairs in this array. We then use the method by Yao et al. (2006) to measure the phase velocity dispersion curve for each cross-correlation. Finally, we use a similar method to Barmin et al. (2001) to invert for the phase velocity map at each period.

Fig. 2a shows an example of the cross-correlations between station PE13 and all the odd number stations on line PE. The cross-correlations are dominantly one-sided because the noise sources are not uniformly distributed, with the strongest on the Pacific Ocean side. The synthetics in Ma et al. (2013) shows that this non-uniform distribution of noise source does not cause a bias in the traveltime of the inter-station surface wave. We can also observe that continuous signals arrive earlier (denoted with green line) or later (denoted with blue line) than the inter-station surface wave. These are due to a scatterer (yellow star in Fig. 2c), which was reported by Ma et al. (2013), and for the purposes of the structure inversion, we ignore these arrivals. For each station pair, we stack the positive and negative time lags of the cross-correlation, and measure the dispersion curve from the stacked waveform (e.g. Fig. 2b for PE13–PE50), following Yao et al. (2006). Two criteria are used in accepting the measurement at certain period. First, the threshold of signal-to-noise ratio (SNR) is empirically set at 5 to eliminate the irregular (e.g. unsmooth) segments of the dispersion curve in noisy period bands. Note that since the ambient noise energy is peaked around 5 s and 15 s, and also because the scattering effect is strongest at short periods, fewer station pairs satisfy the SNR criterion at longer or shorter periods. Second, the maximum wavelength λ (and hence the maximum period) is limited by the inter-station distance Δ (usually $\Delta \geqslant 3\lambda$) in order to satisfy the far field approximation in the measurement procedure (Lin et al., 2008; Yao et al., 2006). This reduces the resolution of the tomographic inversion for longer periods, and because of these restrictions, we only use the ambient noise measurements from 6 s to 25 s period.

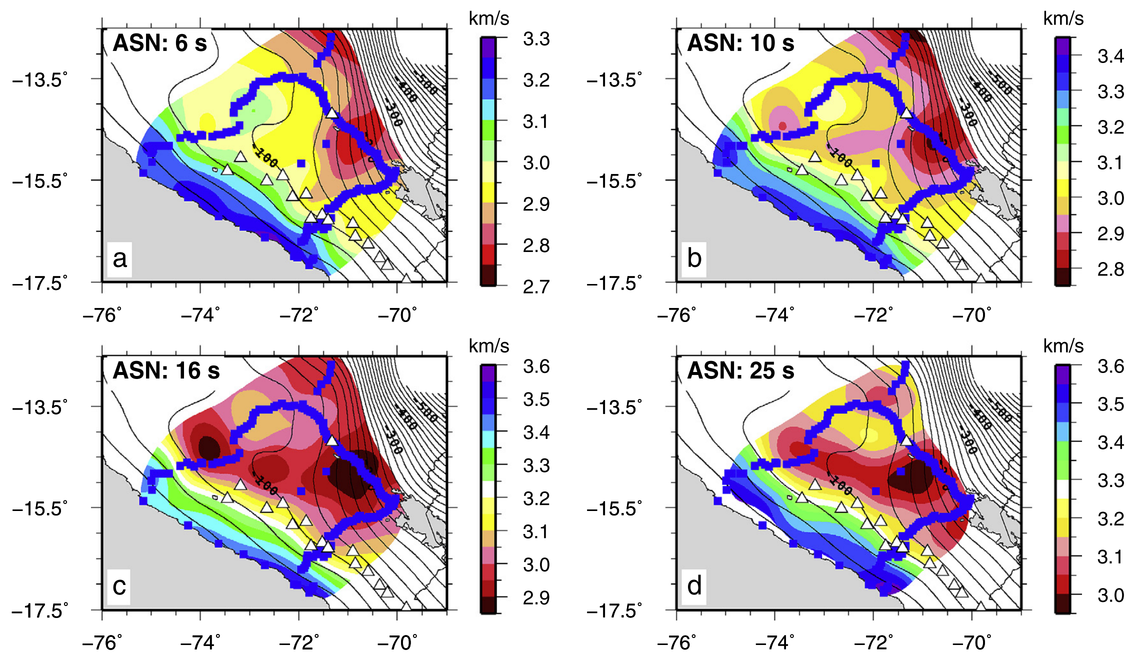

Fig. 3. Ambient noise phase velocity maps at 6, 10, 16 and 25 s periods. The results are clipped with model error less than 10% of the average velocity in each period.

The phase velocity maps at each period are inverted from the inter-station dispersion measurements. The region is discretized into a $0.5° \times 0.5°$ grid, and for each period, a linear inversion for the slowness model is done using the method of Barmin et al. (2001). The penalty function includes the data misfit and model smoothness, as well as constraints on model curvature in order to be consistent with the earthquake method (Forsyth and Li, 2005; Yang and Forsyth, 2006a, 2006b), which is discussed in Section 2.2. For the smoothness term, the correlation length (σ in the Gaussian function) is set at 1°, and we use the trade-off curve between misfit and model smoothness (Aster et al., 2012; Hansen, 1992) to determine the regularization parameter. For the curvature term, the regularization parameter is calculated to minimize (in least squares sense) the off-diagonal terms of model covariance matrix. Two iterations are performed. With the first iteration, all data are equally weighted, and we also apply heavy damping, which results in a highly smoothed model. For the second iteration, the data are weighted inversely proportional to their misfits in the first iteration. The i-th diagonal element of the data covariance matrix is specified as $\max(e_i, w)^2$, where e_i is the misfit of the i-th data after the first iteration, and w is the water level cutoff to ensure stability. The resulting slowness map is then converted to the phase velocity map, which is shown in Fig. 3.

The resolution and model error at two representative periods – 6 s and 25 s – are shown in Supplementary Fig. 1. Due to the small size of the problem, we can directly use the resolution matrix $R = (G^T C^{-1} G + Q)^{-1} G^T C^{-1} G$ (where C is the data covariance matrix, Q is the regularization matrix, and G is the forward operator on the slowness model) from the inversion above to generate standard checkerboard resolution maps. Here, the input model contains ±10 percent perturbations of the average velocity, and the output model (expressed in percentage) is shown in Supplementary Fig. 1a–b. The error of the model is estimated from the diagonal elements of the model covariance matrix, which is approximately $C_{mm} = (G^T C^{-1} G + Q)^{-1}$ and is typically smaller than 0.05 km/s inside of the array (Supplementary Fig. 1c–d). The model error reflects the variance of the model subject to the variance of the data, and does not reflect the deviation from the true model where the resolution is low.

2.2. Earthquake two-plane wave

The earthquakes we used are selected from the NEIC catalog, using a search window with magnitude larger than 6.0, depth less than 100 km, and epicentral distance in the range of 30–120° (Supplementary Fig. 2). We used the "two-plane-wave method" (Forsyth and Li, 2005; Yang and Forsyth, 2006a, 2006b) to determine the phase velocity structure from 25–67 s period. With this method, the incoming wavefield from one earthquake is represented by the superposition of two plane waves, each with unknown amplitude, initial phase and direction. This approximately accounts for multipathing and the off-great circle path of the surface wave (e.g. Cotte et al., 2002). From the amplitude and phase information recorded by an array of stations, we are able to invert for those wave parameters and the local phase velocity structures as well as other parameters such as site amplification and 1-D attenuation.

In processing the data, we first visually inspect all the data and delete those with obvious recording problems or complex waveforms. The data are then filtered with a series of narrow band-pass (10 mHz), zero-phase, fourth-order Butterworth filters centered at the periods of 25, 29, 33, 40, 45, 50, 59 and 67 s. We then window the surface wave part of each seismogram. The window length is 200 s for periods less than 60 s, and 300 s for 67 s. A 50 s half-cosine taper is added to each end of the window. To find the center of the window, we first measure the group velocity dispersion curve for each station, which gives the arrival time of the surface wave envelope at each period. These estimates are further refined by comparing all the stations for one event. Finally, from the windowed seismograms, the amplitude and phase information is determined. In the inversion procedure, a finite-frequency kernel (Zhou et al., 2004) is used for each period, instead of an empirical Gaussian kernel as was used in the ambient noise tomography.

The nonlinear inversion is linearized to iteratively solve for corrections to the current model. We first discretize the region into a $1° \times 1°$ grid, and do the inversion starting from a uniform model estimated from Crustal2.0 (Laske et al., 2001). The results are then used to calculate an updated uniform starting model for a second inversion, which is on a $0.5° \times 0.5°$ grid (Fig. 4). In addition to a uniform starting model, we also test a starting model with patterns

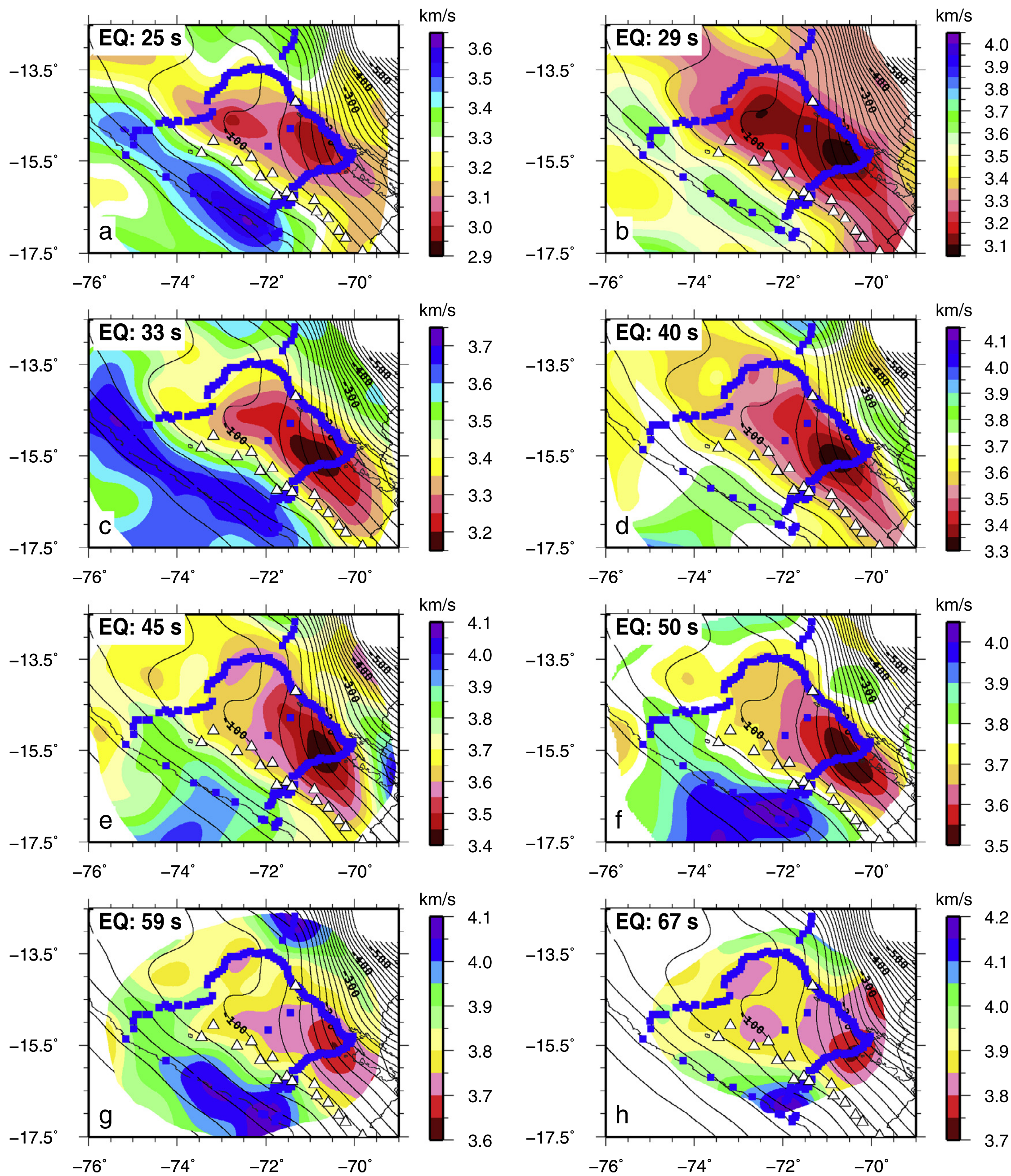

Fig. 4. Two-plane-wave phase velocity maps from 25 s to 67 s period. The results are clipped with model error less than 10% of the average velocity in each period.

from the results of $1^\circ \times 1^\circ$ inversion. The main features are consistent, and hence the initial model does not affect the shear wave inversion results discussed in the following section.

The model resolution and model covariance matrices obtained in the last iteration is used to evaluate the model standard error (Supplementary Fig. 3). Since we solve for the perturbation Δm to the current model in each iteration, the error and resolution is that of Δm. However, if we assume in the $(n-1)$th iteration, the resulted model m_{n-1} is close enough to the global optimum, which means there is no error associated with the starting model in the nth iteration, then the error and resolution of Δm represents that of m_n. If the iteration converges to a local optimum, then the error can be underestimated, but as addressed above, we tested two starting models to check the consistency. We also check the consistency between the ambient noise and the earthquake surface wave results at the overlap period of 25 s (Supplementary Fig. 3e). We see that the difference is generally less than 0.05 km/s inside of the box array, but is larger outside of the box where we do not have good resolution for both methods. The earthquake result is possibly more reliable outside of the box since it reflects the rapid change in topography (Fig. 1). Nevertheless, we use the average of the results from the two methods at 25 s.

2.3. Inversion for shear velocity structure

With the phase velocity maps, we are able to extract the phase velocities from 6 to 67 s period at each location. The 1-D shear velocity structure at each location is inverted from the estimated dispersion curve using the linearized inversion algorithm by Herrmann and Ammon (2004). These 1-D profiles are then combined to form a 3-D structure of the whole region.

For each 1-D inversion, we invert for a smooth model without a Moho discontinuity because the surface waves are not very sensitive to discontinuities, and also we do not have a direct estimate of Moho depth inside of the "box" array. The effects of not imposing a Moho in the inversion will be addressed later. The crustal thicknesses (Fig. 5) and Poisson's ratio beneath the four lines of the array, which are around the edge of the "box", were previously determined from receiver function studies (Phillips and Clayton, 2014; Phillips et al., 2012). Although the Vp/Vs ratio measured by the receiver function analysis is only for the crust, we use the average values of 1.76 for the forearc and 1.75 for the backarc (Phillips and Clayton, 2014; Phillips et al., 2012) for the whole depth during the inversions. We found that the surface wave inversion is not very sensitive to the particular choice of Vp/Vs ratio.

We initially invert for the average structures of the forearc and backarc regions separately (Fig. 6). We define the 3.35 km/s contour in the 25 s phase velocity map (Fig. 4a) as the boundary between the two regions. The top 60 km is discretized into 5 km layers, and then 10 km layers to 140 km depth. We also tested the case with the combination of 10 km and 20 km layer thicknesses with no significant differences in the results. Two smooth starting models (Fig. 6a–b) were tested. One is a uniform model of 4 km/s, the other is a model linearly increasing from 3.5 km/s at 0 km to 4.5 km/s at 140 km depth. The damping parameter is chosen as 0.5, from the trade-off curve of the misfit and model smoothness (Hansen, 1992), and the density is fixed at 3 kg/m^3. The inversion as shown in Fig. 6a–b is stable under the two starting models, except for the velocities from below 120 km depth. From the dispersion curves predicted by the two starting models (Fig. 6e), we see that the linear-gradient initial model (model b) has a better fit at 67 s period. This suggests that the uniform initial model with 4 km/s is too slow at greater depths implying that the inversion is trapped in a local minimum, and hence the linear-gradient initial model is preferred. The average structures for the forearc and backarc regions (Fig. 6b) are then used as starting models for the inversions with finer x–y grids. A damping parameter of 1.0 is used in the results shown here, although other values are also tested. Several depth slices are shown in Fig. 7.

To show the effects of Moho on the inversion results, in Fig. 6c, we also tested a case with a velocity discontinuity in the initial model. The depth of the discontinuity corresponds to the average Moho depth of the forearc and backarc region estimated from the receiver function studies (Fig. 5). We see that with equivalent misfit to the dispersion curves (Fig. 6e), significant differences (>0.05 km/s) exist in the velocities of the lower crust and upper mantle between the two inversion results with or without a Moho (Fig. 6d). Nevertheless, the smoothed model is determined by the true velocities of the lower crust and upper mantle, and therefore

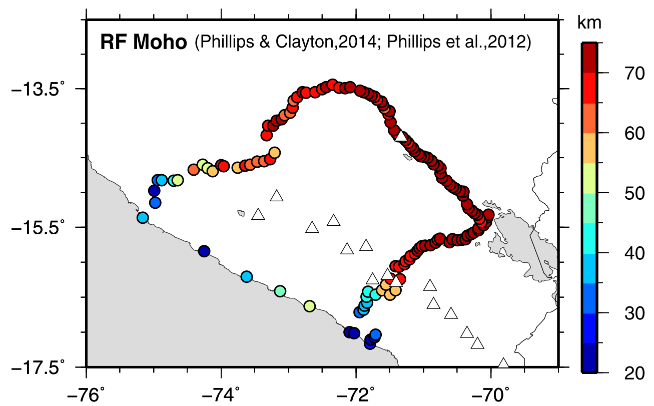

Fig. 5. The Moho depth from receiver functions (Phillips and Clayton, 2014; Phillips et al., 2012).

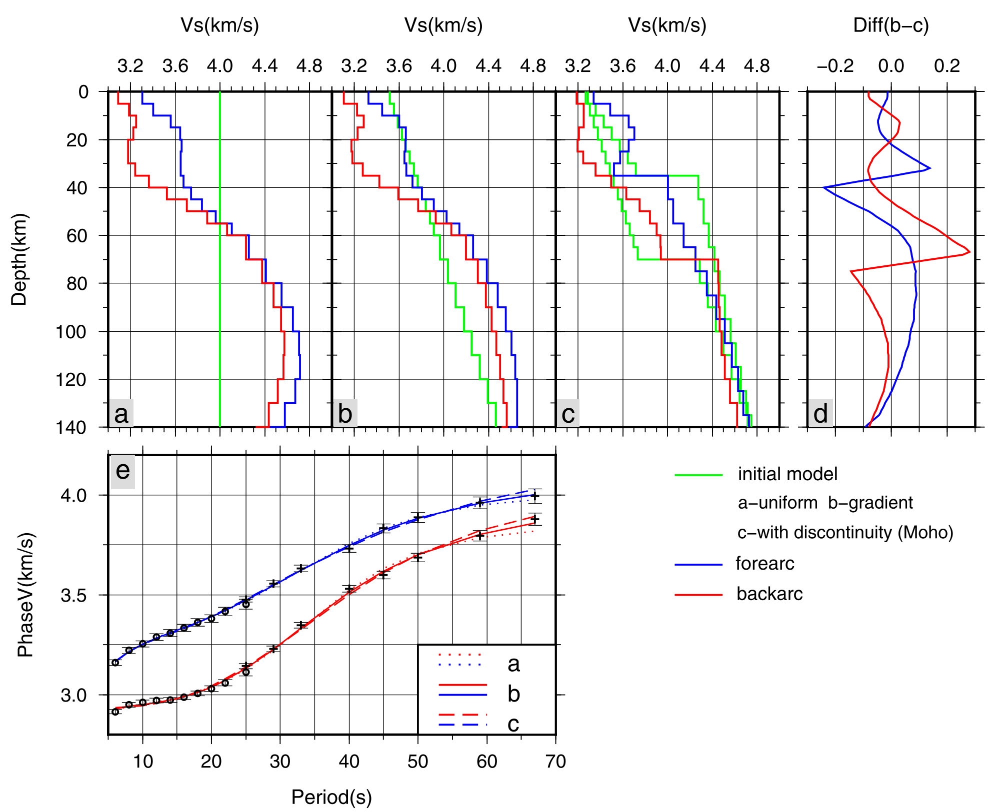

Fig. 6. (a–c) Inversion results from different starting models. The green lines are the starting models. The blue and red lines are inversion results for the forearc and backarc regions respectively. (d) The difference between the results in Panels b and c. (e) Average dispersion curves for the forearc and backarc regions respectively. The data are plotted with error bars, and the predictions are from the inversion results in Panels a–c. (For interpretation of the references to color in this figure legend, the reader is referred to the web version of this article.)

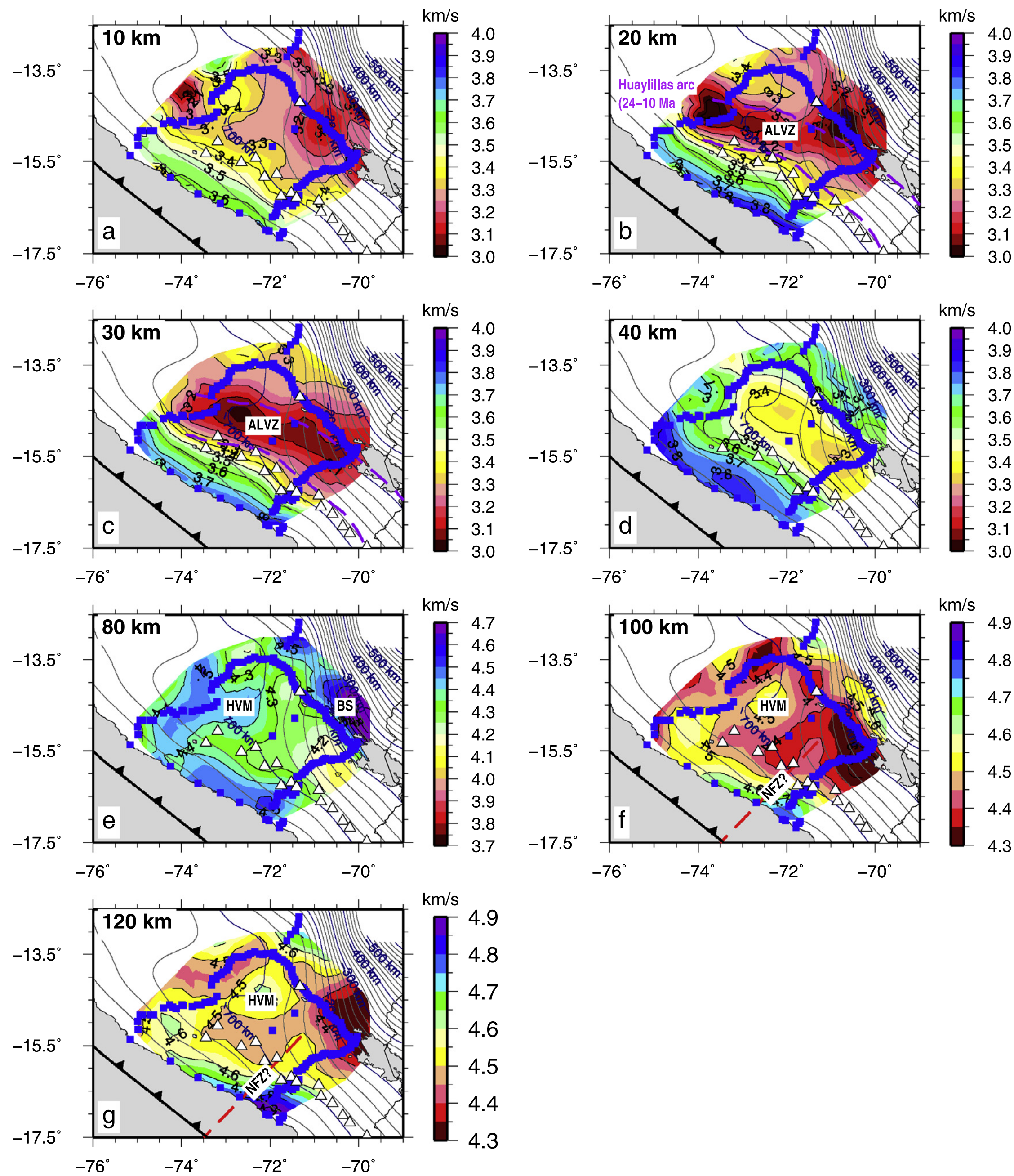

Fig. 7. The depth slices of the shear wave velocity structure from 10 km to 120 km depth. ALVZ: the Andean Low-Velocity Zone; HVM: the High Velocity Mantle above the flat slab; BS: the Brazilian Shield; NFZ: the Nazca Fracture Zone.

the velocity contrasts among the smooth models in each location do reflect the first order features and will be discussed in the next section.

3. Results and discussions

3.1. The mid-crust structure

A mid-crust low-velocity zone is shown clearly in the 20 km and 30 km depth slices ("ALVZ" in Fig. 7b–c). From the cross-sections (Fig. 8), we see that the low-velocity zone extends from 20 km to about 35 km depth. We can also observe this structure directly from 10–25 s phase velocity maps (Figs. 3b–d, 4a).

Interestingly, the low-velocity zone is oblique to the trench, and does not coincide with the present volcanism. Instead, the location and shape of it coincides well with the extent of the Huaylillas arc (24–10 Ma) in Mamani et al. (2010), as shown in Fig. 7b–c. We identify it as part of the Andean low-velocity zone, which has been imaged by the receiver function study in the latitude range of 20°S–26°S (Yuan et al., 2000). Although the amplitude and thickness of this low-velocity zone varies with location, our results match the structure profile at 24°S, and is explained as the partially molten rocks in the crust. The crustal melting is also characterized by high seismic attenuation, reduced seismic velocity, and high conductivity as shown in several other seismic and, magnetotelluric and geomagnetic deep-sounding experiments in the Central Andes (Schilling et al., 2006). The macroscopic properties, such as elasticity and conductivity, depend not only on the volume fraction of the melt (liquid), but also on the microscopic geometry of the liquid phase (Hashin and Shtrikman, 1962; Takei, 1998). On the assumption that the melts form an ideally interconnected network, the observed electrical conductivity pro-

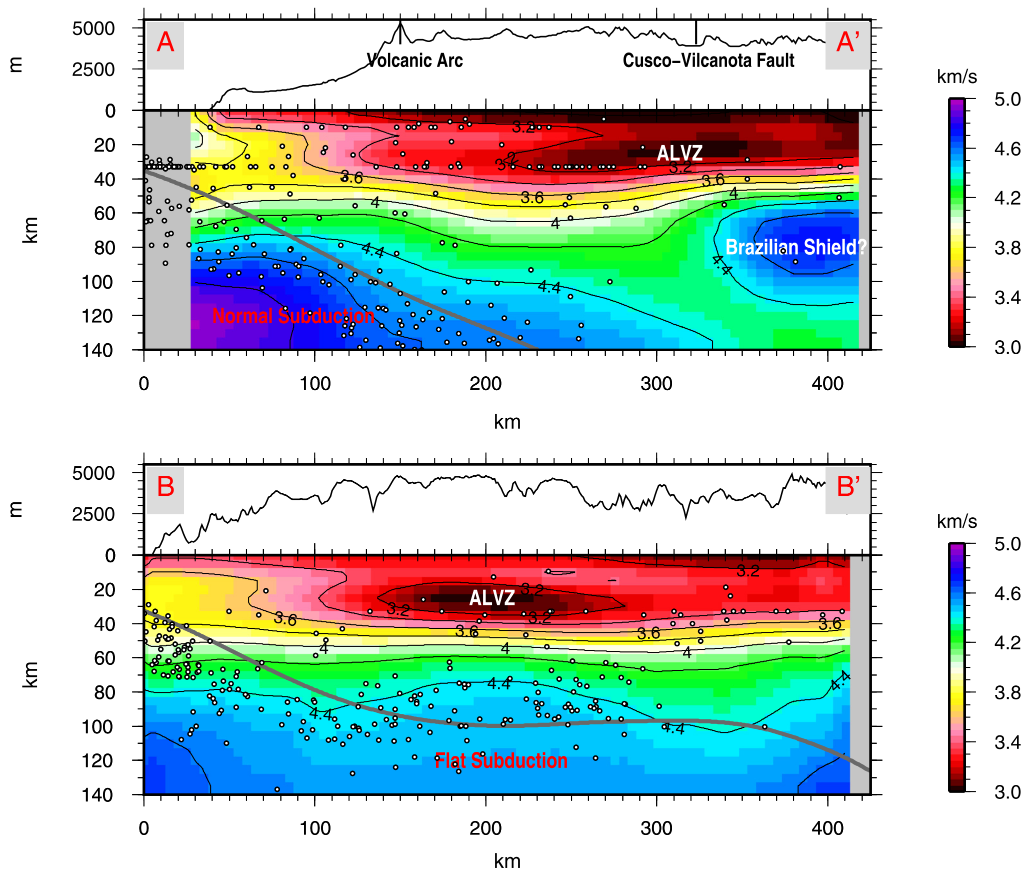

Fig. 8. The shear wave velocity structure along A–A′ and B–B′ profiles in Fig. 1. The earthquakes are from NEIC catalog (1976/01–2013/09), and those within ±60 km are projected to the profile. The slab1.0 model (http://earthquake.usgs.gov/research/data/slab) is plotted in dark gray lines.

vides a minimum estimation of the proportion of melts to be 14–27 vol.% (Schilling et al., 2006). In order to do the estimation from the shear wave velocity results, we need to understand the dependence of shear wave velocity on the temperature and distribution of the melts.

Because of the correlation between the ALVZ and the surface exposure of the volcanic rocks, Yuan et al. (2000) suggest that this feature is most probably caused by mantle magmatism and heat advection related to subduction, lithospheric mantle delamination and intracrustal diapirism. As suggested in Kay and Coira (2009) and Ramos and Folguera (2009), the steepening of the Oligocene flat slab beneath the Altiplano plateau and the early Miocene flat slab beneath the Puna pleateau can lead to the continuous mantle and crustal melting that produced widespread volcanism (including large ignimbrites) in the Central Andes. The magmatic addition from the mantle, although is not significant to the crustal thickening compared with the tectonic shortening (Allmendinger et al., 1997), contributes heat, which induces the crustal melting and lowers the viscosity of the mid-lower crust, and therefore controls the mechanical behavior of the crust. For example, the low velocity zone can be a channel for the crustal flow, which is a proposed mechanism for thickening the Altiplano crust (Husson and Sempere, 2003). The low-velocity zone we observed probably delineates the arcs formed during the steepening of the ancient Altiplano flat slab, and hence maps the geometry of the ancient flat slab at its northern end.

3.2. The slab velocity

The age of the subducted Nazca slab at the trench is about 50 Ma (Müller et al., 2008), and therefore the thickness of it is estimated to be 80 km from the Pacific model in Zhang and Lay (1999). With the slab contours which delineate the top of the oceanic lithosphere, we can estimate that the bottom of the oceanic lithosphere changes from 80 km depth in the trench to 180 km depth beneath the volcanic arc. From the depth slices of 100 and 120 km in Fig. 7, we observe a decrease in the slab velocity from SE to NW in the forearc region. This feature is also evident in the 100 km depth slice of a larger scale surface wave tomography of South America (Feng et al., 2007). The decrease in the shear wave velocity of the slab towards the flat subduction regime coincides with the thinning of the effective elastic thickness (T_e) (Pérez-Gussinyé et al., 2008). Although the age of the slab decreases northwards along the trench (Fig. 1), and shear velocity of the slab generally increases with the age, the difference in the age is not sufficient to explain the velocity difference according to the age-velocity relations (Stein and Stein, 1992; Zhang and Lay, 1999). There is also a velocity contrast, which is clearest in the 120 km depth slice, seemingly indicates the trace of the Nazca fracture zone (Fig. 7g). Again, the age difference of ∼5 Myrs across the fracture zone (Fig. 1) is not sufficient to explain this contrast. The general decrease in the slab velocity northward along the coast appears to be related to the serpentinization during the formation of the Nazca Ridge. Fractures formed during the formation of the Nazca ridge as a hotspot trace (Pilger and Handschumacher, 1981) enable the hydration and serpentinization of the upper mantle of the slab, which lowers the slab velocity. This effect is expected to decrease away from the ridge, which agrees with our observations. The hydration of the slab would provide more buoyancy compared with that of a thickened crust in a ridge (Porter et al., 2012). This study does not extend far enough to the north to address the interesting question of why the slab remains flat after the passage of the Nazca Ridge.

3.3. The mantle above the slab

In the 80–120 km depth slices of Fig. 7, the cold oceanic lithosphere is shown as high velocity in the forearc. We also see a high velocity feature in the mantle above the flat slab ("HVM" in Fig. 7e–g), near the sharp-bending of the slab contours. In local studies of the Pampean flat subduction regime, similar phenomenon is also observed by both body wave (Wagner et al., 2005) and surface wave tomography (Porter et al., 2012). In the area at 72.5°W/13.5°S, where the slab inside of the array is flattest, the velocity is similar as the normal subduction regime, which is possibly due to some local structure. The existence of a comparatively high shear wave velocity mantle above the flat slab indicates a cold environment and the lack of melting, which explains the cessation of the volcanism above it.

3.4. The underthrusting Brazilian shield

We observe a velocity contrast across the PF line, which coincides with the Cusco–Vilcanota Fault System (Fig. 1). A higher velocity block is located to the northeast, and is most prominent in the depth range of 40–100 km (Fig. 7). We note that, because the resolution outside of the "box" array is from the earthquake two-plane-wave method which starts from 25 s, we do not have resolution outside of the "box" shallower than around 30 km depth. Therefore, it's possible that the velocity contrast exists even in the shallow depths. From the cross-section of the normal subduction area (Fig. 8), we see the high velocity is most evident in the uppermost mantle depth. The amplitude of this anomaly in the flat subduction regime is, however, much weaker compared with that in the normal subduction regime (Fig. 7e).

The velocity contrast across the Cusco–Vilcanota Fault System delineates two lithospheric blocks, which is also evident in the geochemical index of mafic rocks (Carlier et al., 2005). The high velocity mantle below the crust of the Eastern Altiplano–Eastern Cordillera is similar as the structure in Bolivia, where it is interpreted as the underthrusting of the Brazilian lithosphere (Beck and Zandt, 2002; Dorbath et al., 1993; Myers et al., 1998). Particularly, the study of Dorbath et al. (1993) to the south of Lake Titicaca, also imaged a velocity contrast, from surface to upper mantle, across a fault near the Lake Titicaca. The underthrusting of the Brazilian shield over time between 19° and 20°S is shown in Fig. 3 in McQuarrie et al. (2005). Our result reveals that the underthrusting Brazilian lithosphere continues northward along the strike. However, since we do not observe a strong velocity anomaly below the Eastern Cordillera in the flat subduction regime, it's possible that either a collision happened between the oceanic lithosphere and the Brazilian lithosphere, or the Brazilian lithosphere hasn't reached the northern part of our imaged area.

4. Conclusions

We have imaged the shear wave velocity (V_{SV}) structure of Southern Peru using the surface wave signals from ambient noise cross-correlations and earthquake data. A low-velocity mid-crust structure is imaged, as part of the Andean low-velocity zone. The recently subducted slab below the forearc shows a decrease in velocity from normal to flat subduction regime that appears to be related with the serpentinization during the formation of the Nazca ridge. A comparatively high velocity mantle is observed above the flat slab, which indicates the lack of mantle melting and consequently the cessation of volcanism above it. A velocity contrast across the Cusco–Vilcanota Fault System is imaged, which delineates two lithospheric blocks. It indicates the underthrusting of the Brazilian shield beneath the Eastern Cordillera in Southern Peru.

Acknowledgements

We thank Prof. Huajian Yao for providing the ambient noise dispersion measurement code, Prof. Don Forsyth for providing the two-plane-wave tomography code, and Dunzhu Li for useful discussions. We also thank the editor and two anonymous reviewers for their helpful comments. This work is supported by NSF (EAR-1045683) and the Gordon and Betty Moore Foundation through the Tectonics Observatory at Caltech (contribution number 257).

Appendix A. Supplementary material

Supplementary material related to this article can be found online at http://dx.doi.org/10.1016/j.epsl.2014.03.013.

References

Abbott, D., 1991. The case for accretion of the tectosphere by buoyant subduction. Geophys. Res. Lett. 18, 585–588.
Allmendinger, R.W., Jordan, T.E., Kay, S.M., Isacks, B.L., 1997. The evolution of the Altiplano–Puna plateau of the Central Andes. Annu. Rev. Earth Planet. Sci. 25, 139–174.
Aster, R.C., Borchers, B., Thurber, C.H., 2012. Parameter Estimation and Inverse Problems. Academic Press.
Barmin, M.P., Ritzwoller, M.H., Levshin, A.L., 2001. A fast and reliable method for surface wave tomography. Pure Appl. Geophys. 158, 1351–1375.
Beck, S.L., Zandt, G., 2002. The nature of orogenic crust in the central Andes. J. Geophys. Res. 107, 2230.
Bensen, G.D., Ritzwoller, M.H., Barmin, M.P., Levshin, A.L., Lin, F., Moschetti, M.P., Shapiro, N.M., Yang, Y., 2007. Processing seismic ambient noise data to obtain reliable broad-band surface wave dispersion measurements. Geophys. J. Int. 169, 1239–1260.
Brenguier, F., Shapiro, N.M., Campillo, M., Nercessian, A., Ferrazzini, V., 2007. 3-D surface wave tomography of the Piton de la Fournaise volcano using seismic noise correlations. Geophys. Res. Lett. 34.
Carlier, G., Lorand, J., Liégeois, J.-P., Fornari, M., Soler, P., Carlotto, V., Cardenas, J., 2005. Potassic–ultrapotassic mafic rocks delineate two lithospheric mantle blocks beneath the southern Peruvian Altiplano. Geology 33, 601–604.
Cotte, N., Pedersen, H., Campillo, M., Farra, V., Cansi, Y., 2002. Off-great-circle propagation of intermediate-period surface waves observed on a dense array in the French Alps. Geophys. J. Int. 142, 825–840.
Dorbath, C., Granet, M., Poupinet, G., Martinez, C., 1993. A teleseismic study of the Altiplano and the Eastern Cordillera in northern Bolivia: new constraints on a lithospheric model. J. Geophys. Res., Solid Earth (1978–2012) 98, 9825–9844.
Feng, M., Van der Lee, S., Assumpção, M., 2007. Upper mantle structure of South America from joint inversion of waveforms and fundamental mode group velocities of Rayleigh waves. J. Geophys. Res., Solid Earth (1978–2012) 112.
Forsyth, D.W., Li, A., 2005. Array analysis of two-dimensional variations in surface wave phase velocity and azimuthal anisotropy in the presence of multipathing interference. In: Seismic Earth: Array Analysis of Broadband Seismograms. AGU, Washington, DC, pp. 81–97.
Gerya, T.V., Fossati, D., Cantieni, C., Seward, D., 2009. Dynamic effects of aseismic ridge subduction: numerical modelling. Eur. J. Mineral. 21, 649–661.
Gutscher, M.-A., 2002. Andean subduction styles and their effect on thermal structure and interplate coupling. J. South Am. Earth Sci. 15, 3–10.
Gutscher, M.A., Olivet, J.L., Aslanian, D., Eissen, J.P., Maury, R., 1999. The "lost inca plateau": cause of flat subduction beneath Peru?. Earth Planet. Sci. Lett. 171, 335–341.
Gutscher, M.A., Spakman, W., Bijwaard, H., Engdahl, E.R., 2000. Geodynamics of flat subduction: seismicity and tomographic constraints from the Andean margin. Tectonics 19, 814–833.
Hansen, P.C., 1992. Analysis of discrete ill-posed problems by means of the L-curve. SIAM Rev. 34, 561–580.
Hashin, Z., Shtrikman, S., 1962. A variational approach to the theory of the effective magnetic permeability of multiphase materials. J. Appl. Phys. 33, 3125–3131.
Herrmann, R. Ammon, C., 2004. Surface waves, receiver functions and crustal structure. Computer Programs in Seismology, Version 3, 30.
Husson, L., Sempere, T., 2003. Thickening the Altiplano crust by gravity-driven crustal channel flow. Geophys. Res. Lett. 30, 1243.
Kay, S.M., Coira, B.L., 2009. Shallowing and steepening subduction zones, continental lithospheric loss, magmatism, and crustalflow under the Central Andean Altiplano–Puna Plateau. Backbone of the Americas: shallow subduction, plateau uplift, and ridge and terrane collision 204, 229.

Laske, G., Masters, G., Reif, C., 2001. CRUST 2.0: a new global crustal model at 2 × 2 degrees. Institute of Geophysics and Planetary Physics, The University of California, San Diego, website: http://mahi.ucsd.edu/Gabi/rem.dir/crust/crust2.html.

Lin, F.-C., Moschetti, M.P., Ritzwoller, M.H., 2008. Surface wave tomography of the western United States from ambient seismic noise: Rayleigh and Love wave phase velocity maps. Geophys. J. Int. 173, 281–298.

Ma, Y., Clayton, R.W., Tsai, V.C., Zhan, Z., 2013. Locating a scatterer in the active volcanic area of Southern Peru from ambient noise cross-correlation. Geophys. J. Int..

Mamani, M., Wörner, G., Sempere, T., 2010. Geochemical variations in igneous rocks of the Central Andean orocline (^{13}S to ^{18}S): tracing crustal thickening and magma generation through time and space. Geol. Soc. Am. Bull. 122, 162–182.

Manea, V.C., Pérez-Gussinyé, M., Manea, M., 2012. Chilean flat slab subduction controlled by overriding plate thickness and trench rollback. Geology 40, 35–38.

McQuarrie, N., Horton, B.K., Zandt, G., Beck, S., DeCelles, P.G., 2005. Lithospheric evolution of the Andean fold-thrust belt, Bolivia, and the origin of the central Andean plateau. Tectonophysics 399, 15–37.

Müller, R.D., Sdrolias, M., Gaina, C., Roest, W.R., 2008. Age, spreading rates, and spreading asymmetry of the world's ocean crust. Geochem. Geophys. Geosyst. 9.

Myers, S.C., Beck, S., Zandt, G., Wallace, T., 1998. Lithospheric-scale structure across the Bolivian Andes from tomographic images of velocity and attenuation for P and S waves. J. Geophys. Res., Solid Earth (1978–2012) 103, 21233–21252.

Ocola, L.C., Meyer, R.P., 1972. Crustal low-velocity zones under the Peru-Bolivia Altiplano. Geophys. J. Int. 30, 199–208.

O'Driscoll, L.J., Richards, M.A., Humphreys, E.D., 2012. Nazca–South America interactions and the late Eocene–late Oligocene flat-slab episode in the central Andes. Tectonics 31.

Oncken, O., Hindle, D., Kley, J., Elger, K., Victor, P., Schemmann, K., 2006. Deformation of the central Andean upper plate system—facts, fiction, and constraints for plateau models. In: The Andes. Springer, pp. 3–27.

Pérez-Gussinyé, M., Lowry, A., Phipps Morgan, J., Tassara, A., 2008. Effective elastic thickness variations along the Andean margin and their relationship to subduction geometry. Geochem. Geophys. Geosyst. 9.

Phillips, K., Clayton, R.W., 2014. Structure of the subduction transition region from seismic array data in southern Peru. Geophys. J. Int. 196, 1889–1905.

Phillips, K., Clayton, R.W., Davis, P., Tavera, H., Guy, R., Skinner, S., Stubailo, I., Audin, L., Aguilar, V., 2012. Structure of the subduction system in southern Peru from seismic array data. J. Geophys. Res., Solid Earth (1978–2012) 117.

Pilger, R.H., Handschumacher, D.W., 1981. The fixed-hotspot hypothesis and origin of the Easter—Sala y Gomez—Nazca trace. Geol. Soc. Am. Bull. 92, 437–446.

Porter, R., Gilbert, H., Zandt, G., Beck, S., Warren, L., Calkins, J., Alvarado, P., Anderson, M., 2012. Shear wave velocities in the Pampean flat-slab region from Rayleigh wave tomography: implications for slab and upper mantle hydration. J. Geophys. Res., Solid Earth (1978–2012) 117.

Ramos, V.A., Folguera, A., 2009. Andean flat-slab subduction through time. In: Special Publications, vol. 327. Geological Society, London, pp. 31–54.

Schilling, F.R., Trumbull, R.B., Brasse, H., Haberland, C., Asch, G., Bruhn, D., Mai, K., Haak, V., Giese, P., Muñoz, M., 2006. Partial melting in the Central Andean crust: a review of geophysical, petrophysical, and petrologic evidence. In: The Andes. Springer, pp. 459–474.

Shapiro, N.M., Campillo, M., Stehly, L., Ritzwoller, M.H., 2005. High-resolution surface-wave tomography from ambient seismic noise. Science 307, 1615–1618.

Skinner, S.M., Clayton, R.W., 2013. The lack of correlation between flat slabs and bathymetric impactors in South America. Earth Planet. Sci. Lett. 371–372, 1–5.

Stein, C.A., Stein, S., 1992. A model for the global variation in oceanic depth and heat flow with lithospheric age. Nature 359, 123–129.

Takei, Y., 1998. Constitutive mechanical relations of solid–liquid composites in terms of grain-boundary contiguity. J. Geophys. Res., Solid Earth (1978–2012) 103, 18183–18203.

Wagner, L., Beck, S., Zandt, G., 2005. Upper mantle structure in the south central Chilean subduction zone (30 to 36 S). J. Geophys. Res. 110, B01308.

Ward, K.M., Porter, R.C., Zandt, G., Beck, S.L., Wagner, L.S., Minaya, E., Tavera, H., 2013. Ambient noise tomography across the Central Andes. Geophys. J. Int. 194, 1559–1573.

Yang, Y., Forsyth, D.W., 2006a. Rayleigh wave phase velocities, small-scale convection, and azimuthal anisotropy beneath southern California. J. Geophys. Res. 111.

Yang, Y., Forsyth, D.W., 2006b. Regional tomographic inversion of the amplitude and phase of Rayleigh waves with 2-D sensitivity kernels. Geophys. J. Int. 166, 1148–1160.

Yao, H., van der Hilst, R.D., de Hoop, M.V., 2006. Surface-wave array tomography in SE Tibet from ambient seismic noise and two-station analysis – I. Phase velocity maps. Geophys. J. Int. 166, 732–744.

Yuan, X., Sobolev, S., Kind, R., Oncken, O., Bock, G., Asch, G., Schurr, B., Graeber, F., Rudloff, A., Hanka, W., 2000. Subduction and collision processes in the Central Andes constrained by converted seismic phases. Nature 408, 958–961.

Zhang, Y.-S., Lay, T., 1999. Evolution of oceanic upper mantle structure. Phys. Earth Planet. Inter. 114, 71–80.

Zhou, Y., Dahlen, F., Nolet, G., 2004. Three-dimensional sensitivity kernels for surface wave observables. Geophys. J. Int. 158, 142–168.